Available online at www.sciencedirect.com

ScienceDirect

Underground Space 24 (2025) 44–59

www.keaipublishing.com/undsp

Research Paper

# Continuum-discrete coupling model for mechanical response analysis of tunnels subjected to non-uniform reverse faulting

Zhenning Ba [a,b], Yao Wang [b], Zhiwei Fang [b], Dongqiao Li [c,*]

[a] *State Key Laboratory of Hydraulic Engineering Intelligent Construction and Operation, Tianjin University, Tianjin 300350, China*
[b] *School of Civil Engineering, Tianjin University, Tianjin 300350, China*
[c] *College of Civil Engineering, Henan University of Technology, Zhengzhou 450001, China*

Received 19 January 2025; received in revised form 1 March 2025; accepted 13 March 2025
Available online 4 July 2025

**Abstract**

In recent decades, there have been numerous reports of damage cases involving tunnels crossing active faults. The mechanical response and failure mechanisms of cross-fault tunnels have become a key issue in the field of tunnel engineering. This study established a continuum-discrete coupling model comprising intact rock mass, fault zones, and tunnel. In this model, the tunnel and intact rock are modeled as continuous media, while the fault zone is modeled as a discrete medium. The non-uniform fault displacement is adopted to simulate the mechanical response and damage patterns of tunnels crossing active faults under reverse faulting. The simulation results are validated by comparison with the damage of Longchi tunnel observed from 2008 Wenchuan earthquake in China, as well as the experimental phenomenon from the model test. The results demonstrate that the proposed coupling model effectively reproduces the tunnel failure modes caused by reverse faulting. In addition, the high consistency between the simulation results and experimental data further confirms computational accuracy and reliability of the coupling model. A parametric analysis based on the Xianglushan tunnel in China is carried out to investigate the effects of fault displacements, fault widths, dip angles and fault zone rock mass qualities on damage patterns of crossing-fault tunnels. This study provides a valuable reference for seismic fortification of the tunnel crossing reverse faults.

*Keywords:* Continuum-discrete coupling model; FDM-DEM method; Non-uniform fault displacement; Tunnel damage; Parametric analysis

## 1 Introduction

Active fault displacement has long been a critical challenge to the safety of tunnel construction and operation in fault zones. Historical seismic events have shown that active fault zones are often high-risk areas for severe damage to tunnels. Post-earthquake observations have revealed that the typical failure modes of tunnels crossing active faults, including misalignment of tunnel axes, longitudinal, circumferential, and oblique cracks in linings, spalling of concrete with exposed reinforcement, segmental misalignment, and even collapse within fault fracture zones (Asakura & Sato, 1998; Owen & Scholl, 1981; O'Rourke & Bonneau, 2007; Prentice & Ponti, 1997; Tian et al., 2022; Wang et al., 2001; Shen et al., 2014; Xin et al., 2024; Yu et al., 2016). Therefore, studying the failure modes and disaster mechanisms of tunnels crossing active faults is crucial, as it can provide valuable insights and references for enhancing the resilience of cross-fault tunnel projects.

Over the past decade, researchers have conducted extensive studies on the failure modes and mechanisms of tunnels under fault displacement through physical model tests and numerical simulations. Physical model tests have been an essential method for objectively understanding the seismic damage characteristics of tunnels crossing active faults (Y. Zhang et al., 2023; Z. Zhang et al., 2023; Li et al., 2023). These tests generally simulate fault

* Corresponding author.
*E-mail address:* dongqiao2008@tju.edu.cn (D. Li).
Peer review under the responsibility of Tongji University

https://doi.org/10.1016/j.undsp.2025.03.005

displacement by fixing one side of the fault and applying pseudo-static displacement on the other side, which can be further divided into 1g tests and centrifuge tests, where $g$ represents the unit of gravitational acceleration. Large number of those tests indicate that the structural damage to tunnels crossing faults is mainly concentrated in the fault plane (FP), where the tunnel structure shows inclination and a network of cracks due to fault shear, and even shear faulting. Damage in the intact rock zones of the hanging and footwalls mainly manifests as inclined cracks and circumferential cracks. Related $1g$ test studies include Q. Wang et al. (2023), T. Wang et al. (2023), Gao et al. (2024), J. Zhang et al. (2024), Zhang et al. (2024a), and Wang et al. (2025). Typical centrifuge test studies include Anastasopoulos et al. (2007), Kiani et al. (2016a, 2016b), Sabagh and Ghalandarzadeh (2020), Cai et al. (2019), Tali et al. (2019), and Liu et al. (2023). It is noting that $1g$ tests typically use relatively large-scale models for experimental analysis, which may better capture the structural details of the tunnels under fault displacement (Gou et al., 2023). However, these tests have limitations in replicating the natural stress state of the geological strata surrounding the tunnel. Instead, centrifuge tests generate an $N$-$g$ gravitational acceleration through high-speed rotation ($N$ denotes the gravity scaling factor in the centrifuge test), allowing a scaled model at a $1/N$ ratio to achieve stress conditions consistent with those of the prototype. Nevertheless, the size and load capacity of the centrifuge are often limited, restricting the scale of the model (Yao et al., 2021a, 2021b).

The rapid advancement in computational performance has established numerical simulation as an indispensable approach (Chen et al., 2023; Fei et al., 2024; Yang et al., 2024a, 2024b). In contrast to physical model tests, numerical simulation offers superior cost-effectiveness and efficiency, with highly controllable parameter settings and the capability to model tunnel responses under diverse fault types and geological conditions. Li et al. (2022) and Wang et al. (2024) developed a sophisticated three-dimensional (3D) finite element model that incorporates detailed structural features of shield tunnels, including lining segments and both transverse and longitudinal bolts, to study the mechanical responses of shield tunnels subjected to normal faulting. Liu et al. (2024) developed a 3D finite element model to study the effects of different lateral pressure coefficients and tunnel cross-sectional geometries on the deformation and failure modes of cross-fault tunnels. Yao et al. (2025) constructed a finite element model of a twin tunnel with cross passages intersecting a fault fracture zone to analyze the failure modes under strike-slip faulting. The study also explored the effects of lateral pressure coefficients, connecting passageway positions, and lengths. Tang et al. (2024) introduced a novel finite element simulation framework that employs submodels and a two-stage modeling approach. In comparison with traditional numerical simulation methods, this framework achieves a computational speed increase of approximately 73% when using the same mesh size. Nevertheless, those conventional continuum methods encounter significant challenges in precisely simulating the discontinuous rupture deformation of fault fracture zones, thereby limiting their ability to assess the response of cross-fault tunnels.

To address this issue, Zhong et al. (2020) utilized cohesive interface elements (COH3D8) to simulate the fault core in the central fault zone, enabling the modeling of fault rupture process. Rahman and Taniyama (2015) utilized a coupled finite element-discrete element method (FEM-DEM) to simulate the response of buried pipelines under fault displacement, where the soil and pipeline were represented by discrete and continuum media, respectively. Ma et al. (2019) and Cui et al. (2022) adopted a coupled finite difference-discrete element method (FDM-DEM) to analyze the responses of tunnels crossing faults. In their study, the rock mass was modeled as discrete media, while tunnels were represented by continuum media, which enabled a more detailed microscopic analysis of the surrounding rock failure modes.

The numerical simulation studies summarized above indicate that adopting continuum-discrete coupling methods could provide more accurate evaluations of the mechanical responses of cross-fault tunnels. In related coupling models (Ma et al., 2019; Cui et al., 2022), tunnels are typically modeled as continuum media, while the rock mass (intact rock and fault fracture zone) is treated as a discrete medium. However, intact rock typically does not exhibit substantial discontinuous deformation, potentially leading to unnecessary computational costs. Additionally, most existing studies simulate fault movement by applying uniform fault displacement at the boundaries of the hanging wall and footwall (Tang et al., 2024; Ma et al., 2019; Rahman & Taniyama, 2015). However, post-earthquake field investigations, such as the S-shaped ground deformation following the 1999 Chi-Chi earthquake and the 2008 Wenchuan earthquake (Fig. 1(a)) (Chang et al., 2015; Wang, 2022), as well as results from laboratory experiments (Fig. 1(b)) (Lin et al., 2007; Ahmadi et al., 2018), demonstrate that non-uniform fault displacement closely matches observations of deformation. This underscores the importance and necessity of considering non-uniform fault displacement in simulations.

To overcome these limitations, this paper proposes a continuous-discrete coupling model for tunnels crossing active faults. In this model, tunnels and intact rock are simulated as continuum media, while the fault fracture zone is modeled as a discrete medium. Non-uniform fault displacement is applied at the boundaries of the rock mass to more accurately simulate the deformation characteristics of the geotechnical body and the failure modes of tunnels subject to reverse fault displacement. The paper is structured as follows: Section 1 provides a comprehensive review of existing research on the mechanical response and damage mechanisms of tunnels under fault displacement. Section 2 introduces the engineering background of the numerical simulations and elaborates on the construction of the

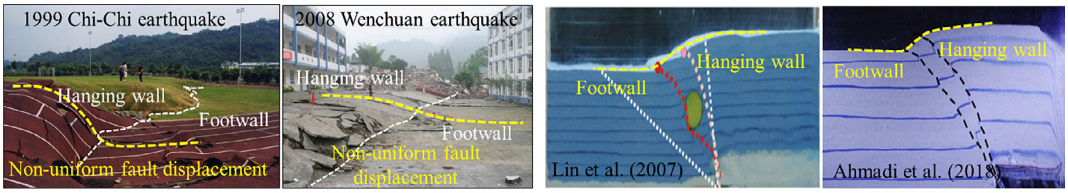


(a) (b)

Fig. 1. Non-uniform fault displacement: (a) observed in the post-earthquake (Chang et al., 2015; Wang, 2022), and (b) observed in the physical model test (Lin et al., 2007; Ahmadi et al., 2018). (Reproduced with permission, courtesy of Elsevier.).

continuum-discrete coupling model. Section 3 validates the model through a model test of cross-fault tunnels. Section 4 conducts a parameter sensitivity analysis and discusses the damage mechanisms of tunnels under reverse faulting.

## 2 Numerical modeling

### 2.1 Engineering background

In this study, Xianglushan Water Diversion Tunnel, a key control project of the central Yunnan water diversion project is selected as background. The tunnel extends over a total length of 63.426 km with a maximum burial depth of 1512 m. The geological conditions along the tunnel are exceptionally complex, characterized by the intersection of three Holocene active faults-the Longpan-Qiaohou Fault (F10), the Lijiang-Jianchuan Fault (F11), and the Heqing-Eryuan Fault (F12)-with its alignment. Historical records indicate that these faults have experienced earthquakes exceeding $M_s$ 6. According to seismic hazard analysis, the peak ground acceleration (PGA) at a 10 % probability of exceedance in 50 years is 0.308$g$, corresponding to a seismic intensity of VIII, which poses significant challenges to both the construction and operation of the project.

The Longpan-Qiaohou Fault (F10) predominantly underwent compressive-thrust movement during the early Cenozoic Era, subsequently transitioning to extensional-strike-slip movement in later stages. The Lijiang-Jianchuan Fault (F11) bifurcates into three branches near the tunnel axis, with the southeastern branch (F11-3, 4) being the principal fault. Specifically, the eastern branch (F11-3) is a significant west-dipping, left-lateral thrust fault. The Heqing-Eryuan Fault (F12) is an active Holocene fault that has exhibited both left-lateral strike-slip and extensional normal faulting since the Quaternary Period. The dip angles of these fault zones range from 50° to 90°, with fault fracture zone widths typically between 10 and 100 m. Tectonic rocks within the fault-affected areas along the tunnel comprise limestone, mudstone, sandstone, basalt, breccia, and fault gouge. The fault fracture zones primarily consist of fault gouge, breccia, cataclasite, and minor bands of powdered rock, all characterized by poor mechanical properties.

The construction of the Xianglushan Tunnel utilizes both tunnel boring machine (TBM) and drill-and-blast methods. TBM is employed in regions with favorable lithology outside the active fault zones, whereas drill-and-blast techniques are used within the active fault zones. In these fault zones, the construction method comprises initial shotcrete support reinforced with rock bolts, followed by secondary cast-in-place concrete lining. The initial support layer has a thickness of 25 cm, while the secondary lining measures 60 cm.

The fault displacement ($\Delta f$) in the Xianglushan Tunnel area is calculated using the surface wave magnitude ($M_s$) based on Eq. (1) (Huang, 2016), where $A$ = –3.10 and $B$ = 0.49 are regression coefficients. The $M_s$ values recorded in the study area range from 5.0 to 7.0, resulting in fault displacements between 0.22 and 2.14 m. For this study, fault displacements are defined within the range of 0.2–2.0 m.

$$\Delta f = 10^{A+B\times M_s}. \tag{1}$$

### 2.2 Continuous-discrete coupling model with cross-fault tunnel

FLAC3D and 3DEC software were adopted for the numerical simulations. FLAC3D, based on the explicit finite difference method, is highly efficient in solving large deformation and nonlinear problems in continuum media. As for 3DEC, the software employs the discrete element method, dividing the study domain into a series of independent rigid or deformable blocks. The motion of these blocks is governed by Newton's second law, with explicit time integration used to iteratively update their motion states and contact behavior.

#### 2.2.1 Coupling model construction

A 3D continuous-discontinuous coupled model was developed based on the engineering context of the Xianglushan Water Diversion Tunnel, as shown in Fig. 2, where FLAC3D was adopted to simulate the tunnel structure and surrounding rock, while 3DEC was adopted to simulate the fault zone (Itasca, 2022a, 2022b). The model dimensions are 100 m in height, 100 m in width, and 300 m in length, and the model consists of three main components: the tunnel structure, intact surrounding rock, and fault zone. The tunnel features a single-layer lining structure with an outer diameter of 10 m and a lining thickness of 0.6 m, modeled using continuous elements.

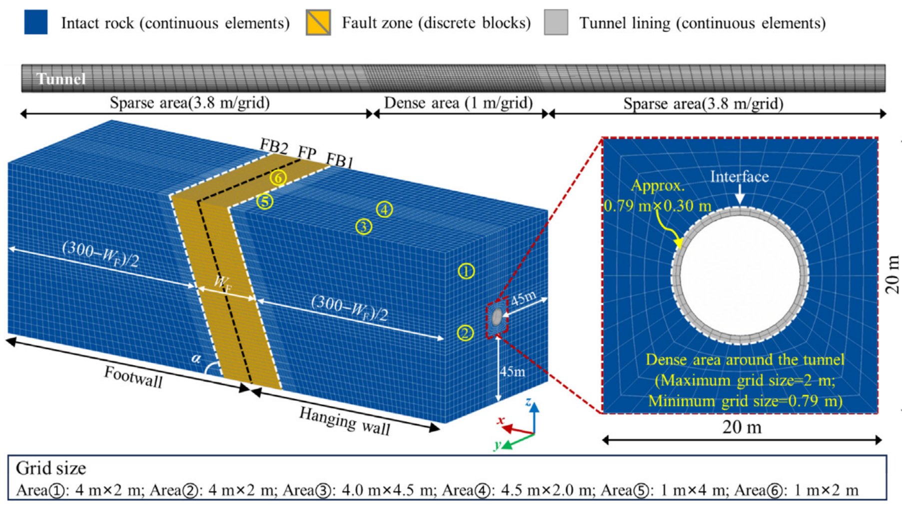

Fig. 2. Coupling model for intact rock-fault zone-tunnel lining systems.

The fault zone was modeled using discrete blocks, where each block is a hexahedron with dimensions of 2 m × 2 m × 1 m. For greater accuracy in calculating internal stress, the blocks were further divided into tetrahedral meshes. The fault zone has a width $W_F$ and a dip angle $\alpha$, with boundaries connecting to the intact rock of the hanging wall and footwall at interfaces FB1 and FB2. The fault core was simplified as an FP located at the center of the fault zone, where sliding occurs between the hanging wall and footwall along the FP during fault displacement.

In grid generation, the tunnel lining was refined longitudinally within the fault-crossing zone and a 10 m range on both sides of the fault (totaling 40 m), with a gird size of 1 m, while the non-refined areas had a grid size of 3.8 m. The cross-sectional grid size of the tunnel was approximately 0.79 m × 0.30 m. Additionally, the surrounding rock within a 20 m × 20 m range around the tunnel (including both intact rock and fault zone) was also refined, with a maximum grid size of 2 m and a minimum grid size of 0.79 m. Other areas grid size can be found in Fig. 2. The coupling model comprised a total of 130 120 continuum element meshes and 52 000 discrete blocks. The mesh convergence analysis is presented in Section 3.

Contact interfaces were introduced between the tunnel and the surrounding rock to simulate relative sliding and separation under fault displacement. The interfaces are collections of triangular interface elements, each of which is defined by three interface nodes. Interface elements are attached to a zone boundary through interface nodes (Itasca, 2022a). In the shear direction, the yield relationship is defined as Eq. (2), where $F_{s,\,max}$ is the maximum shear force, $A_{int}$ is the area of interface elements, $c_{int}$ is the cohesion along the interface, and $\varphi_{int}$ is the friction angle of interface. In the normal direction, the yield relationship is defined as Eq. (3) (Itasca, 2022a), where $F_{n,max}$ is the maximum tensile force, and $\sigma_t$ is the tension strength of interface. When the shear force, $F_s > F_{s,max}$, relative sliding occurs between tunnel and intact rock. When the tensile force, $F_n > F_{n,max}$, separating occurs between tunnel and intact rock. In this study, $\sigma_t$ is set as 0, which means that there is only compression behavior and no tensile behavior on the interface between the tunnel and rock mass. The parameters of interface are listed in Table 1, where $k_n$ and $k_s$ are the normal and shear stiffness, which can be calculated by Eq. (4) (Itasca, 2022a), where $K$ and $G$ are the bulk and shear modulus, respectively; $\Delta z_{min}$ is the smallest width of an adjoining zone in the normal direction.

In the coupling model, the mechanical interactions at the fault zone-tunnel and fault zone-intact rock interfaces are governed by the continuum-discrete coupling method. This method is a numerical technique that coordinates mechanical responses between continuous and discrete media. It establishes spatial correspondence between discrete block vertices and continuous element faces, facilitating the transfer of grid point velocities from the continuous medium to the discrete medium and the feedback of vertex forces from the discrete medium to the continuous medium, thereby achieving mechanical coupling. A detailed description of the coupling continuum-discrete coupling process is presented in the Section 2.2.2.

$$F_{s,max} = c_{int}A_{int} + \tan\varphi_{int} \cdot F_n, \tag{2}$$

$$F_{n,max} = \sigma_t A_{int}, \tag{3}$$

$$k_n = k_s \le 10\left\{\max\left[\frac{(3K+4G)}{3\Delta z_{min}}\right]\right\}. \tag{4}$$

Table 1
Mechanical properties of the rock-tunnel interface.

| Interface properties | Value |
|---|---|
| $k_n$ (GPa/m) | $1.2 \times 10^{11}$ |
| $k_s$ (GPa/m) | $1.2 \times 10^{11}$ |
| $c_{int}$ (MPa) | 1.1 |
| $\varphi_{int}$ (°) | 39 |

### 2.2.2 Continuous-discrete coupling process

The coupling between the continuous and discrete media occurs at the interface between the fault zone and the intact rock of the hanging wall and footwall. As illustrated in Fig. 3, the coupling between continuous elements (FLAC3D) and discrete (3DEC) blocks is facilitated through a boundary weight mapping, enabling effective data exchange. This process consists of two primary stages: the Step 1 involves checking for coplanarity between the faces of the continuous elements and the vertices of the blocks, while the Step 2 focuses on calculating the weights for each block vertex based on its relative position to the four grid points on the continuous element boundary face. These weights are computed by determining the area ratios formed between the block vertices and the grid points, relative to the total area of the continuous element face. During each time step, the velocities of the grid points are weighted and aggregated to update the block vertices, and the reaction forces from the blocks are transferred back to the grid points. This ensures consistent mechanical data exchange between continuous elements and discrete blocks.

The interaction between individual blocks is governed by joints characterized by the normal and shear stiffness ($k_n$ and $k_s$), joint cohesion ($c_j$), and joint internal friction angle ($\varphi_j$). If the normal or shear stress at a joint exceeds its tensile or shear strength, adjacent blocks will undergo separation or sliding. The normal and shear stiffness ($k_n$, $k_s$) of the contact surfaces between discrete blocks can also be calculated using Eq. (4). In the shear direction, when the normal stress ($\sigma_n$) exceeds the tensile strength ($S_t$), the normal stress degrades to zero, resulting in block separation. In the shear direction, when the shear stress reaches peak strength, the peak shear stress is given by Eq. (5) (Itasca, 2022b). When the peak shear strength is exceeded, the shear strength drops instantaneously to the residual shear strength. The residual strength $S_{res}$ is given by Eq. (6) (Itasca, 2022b), where $c_{j,res}$ is the residual cohesion, and $\varphi_{j,res}$ is the residual friction angle. By default, $c_{j,res} = 0$ and $\varphi_{j,res} = \varphi$.

$$S = c_j + \sigma_n \tan \varphi_j, \tag{5}$$

$$S_{res} = c_{j,res} + \sigma_n \tan \varphi_{j,res}. \tag{6}$$

### 2.2.3 Non-uniform displacements and boundary conditions

As noted in the introduction, most current studies simulate reverse faulting using uniform fault displacement, which fails to accurately reflect the S-shaped deformation of strata observed in post-earthquake investigations. To address this, this study adopted the non-uniform fault displacement model proposed by Zhang et al. (2024b), which accounts for the influence of fault width on displacement, to simulate the reverse fault movement, as shown in Eqs. (7)–(10), where $\Delta f_h$ and $\Delta f_f$ represent the fault displacements of the hanging wall and footwall, respectively; $\Delta f_{h,max}$ and $\Delta f_{f,max}$ denote the maximum fault displacements of the hanging wall and footwall, respectively; $x$ represents the horizontal distance from any position on the hanging or footwall to the fault plane; $i_h$ and $i_f$ are the displacement response coefficients of the hanging wall and footwall, respectively; and $W_F$ is the fault width. It is important to emphasize that the simulation assumes relative motion between the hanging wall and footwall, with the maximum fault displacements $\Delta f_{h,max}$ and $\Delta f_{f,max}$ both set as 1 m.

$$\Delta f_h = \Delta f_{h,max}\left(1 - 0.99 \times 9.28^{\frac{x}{i_h}}\right), \tag{7}$$

$$\Delta f_f = -\Delta f_{f,max}\left(0.99 \times 0.16^{\frac{x}{i_f}} + 1\right), \tag{8}$$

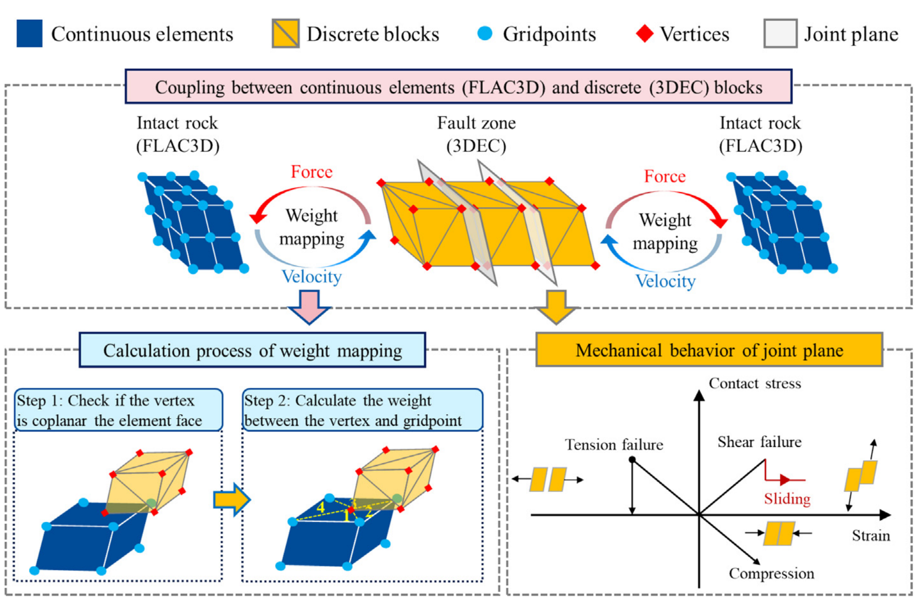


Fig. 3. Coupling process between continuous elements (FLAC3D) and discrete (3DEC) blocks, and the mechanical behavior of joint plane.

$$i_h = 11.09\Delta f_{h,max}^{0.44} + \frac{W_F}{2}, \tag{9}$$

$$i_f = 11.09\Delta f_{f,max}^{0.44} + \frac{W_F}{2}. \tag{10}$$

The numerical simulation is conducted in two steps: Step 1-initial stress equilibrium, and Step 2-simulation of reverse faulting, as illustrated in Fig. 4. During the initial stress equilibrium phase, the bottom of the model is fixed vertically, while vertical stress $\sigma_z$ is applied at the top. Normal stresses $\sigma_x$ and $\sigma_y$ are applied on all lateral sides, with the normal stress linearly increasing with depth to reflect the actual stress conditions in the field. The values of the vertical and horizontal stresses are referenced from Liu et al. (2023), with $\sigma_z = 4$ MPa, and $\sigma_x = \sigma_y = 2$ MPa. Applying confining pressure is crucial for discrete blocks, as it significantly enhances the contact tightness and friction between blocks, effectively improving fault displacement transmission within the fault zone. After generating the initial stress field, non-uniform fault displacement is applied at the bottom of the hanging wall and footwall, whereas uniform displacements are applied at the right and left lateral boundaries. Rolling supports are installed on boundaries perpendicular to the $y$-axis to restrict overall movement of the model in the $y$-axis.

#### 2.2.4 Material constitutive models and parameter setting

The classical Mohr–Coulomb model is widely used in rock mass mechanical behavior simulations due to its simplicity, requiring fewer parameters and easy implementation, this model exhibits limitations in capturing failure and strain-softening behavior of rock mass. Despite its limitations, the Mohr–Coulomb model is employed in this study as it effectively captures the essential nonlinear mechanical behavior of rock masses. The mechanical response of rock mass is influenced by parameters such as Young's modulus ($E$), density ($\rho$), Poisson's ratio ($v$), cohesion ($c$), and internal friction angle ($\varphi$). For the joints within the fault zone, the Coulomb slip model was used. The values of the joint internal friction angle and cohesion are referenced from Zhang et al. (2020). The parameters for the rock mass and the joints are listed in Table 2.

A modified concrete elastoplastic damage model is employed to simulate the damage to the tunnel structure, which utilizing the concepts of fracture-energy-based damage and modulus degradation in continuum damage mechanics. The parameters of concrete damage model are provided in the Table 3 (Itasca, 2022a), where $\psi$ is dilation angle; $f_c$ and $f_t$ are the maximum uniaxial compression and tension strengths; $f_{c0}$ and $f_{t0}$ are initial yield compression and tension strengths; $G_c$ and $G_t$ are fracture energies in uniaxial compression and tension states; $L_c$ and $L_t$ are reference lengths in uniaxial compression and tension states; $d_c$ and $d_t$ are damage parameters for compression and tension.

## 3 Model validation

### 3.1 Mesh convergence analysis

Six meshing generation cases were designed to conducted the mesh convergence analysis, which were listed in Table 4. It should be noted that the model presented in Section 2 corresponds to meshing case 4. Figure 5 illustrates the variation curves of the vertical displacement at the tunnel crown under different mesh densities. The results demonstrate that when the total number of elements reaches 182 120, further increasing the element count has a negligible impact on the vertical displacement of the tunnel vault, and the displacement values gradually stabilize. Considering the balance between computational accuracy and efficiency, case 4 adopted in this study ensures sufficient accuracy while maintaining high computational efficiency, making it the optimal mesh generation strategy.

### 3.2 Validation through experimental data and the seismic damage of Longchi tunnel

To further validate the accuracy of the coupling model in simulating the mechanical response of tunnel, a 3D cou-

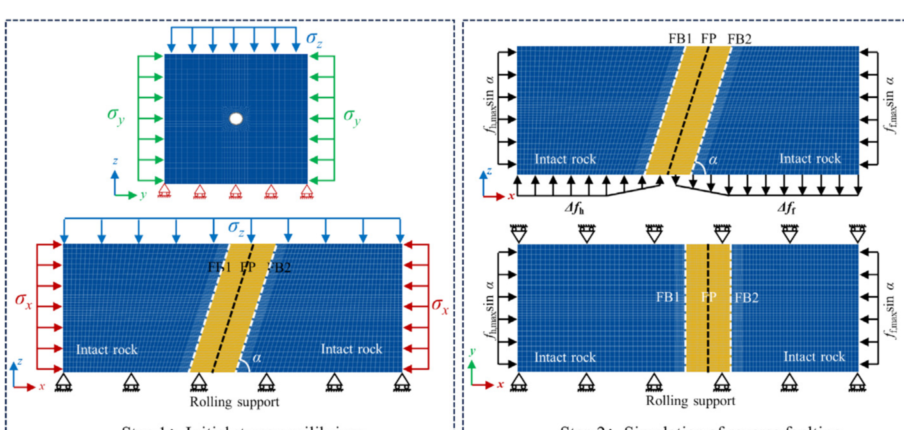


Fig. 4. Boundary conditions in each simulation step.

Table 2
Mechanical parameters of rock masses and joints.

| Media | Rock mass mechanical parameters | | | | | Joint mechanical parameters | | | | |
|---|---|---|---|---|---|---|---|---|---|---|
| | $E$ (MPa) | $v$ | $\rho$ (kg·m$^{-3}$) | $c$ (MPa) | $\varphi$ (°) | Joints | $k_n$ (GPa/m) | $k_s$ (GPa/m) | $c_j$ (MPa) | $\varphi_j$ (°) |
| Intact rock | 7500 | 0.28 | 2900 | 1.10 | 45 | $J_{FP}$ | 10 | 10 | 0.025 | 7 |
| Fault zone | 1500 | 0.33 | 2100 | 0.15 | 32 | $J_{FZ}$ | 10 | 10 | 0.075 | 25 |

Table 3
Mechanical parameters of tunnel (Itasca, 2022a).

| $E$ (GPa) | $v$ | $\psi$ (°) | $f_c$ (MPa) | $f_{c0}$ (MPa) | $G_c$ (MN/m) | $L_c$ (m) | $d_c$ |
|---|---|---|---|---|---|---|---|
| 31.5 | 0.2 | 20 | 27.6 | 16.04 | 0.056 | 0.0826 | 800 |
| $f_t$ (MPa) | $f_{t0}$ (MPa) | $G_t$ (MN/m) | $L_t$ (m) | $D_t$ | | | |
| 3.48 | 3.48 | 40 | 0.0826 | 3000 | | | |

Table 4
Simulation cases of mesh convergence analysis.

| Meshing case | Continuous elements | Discrete blocks | Total |
|---|---|---|---|
| 1 | 60 864 | 13 568 | 74 432 |
| 2 | 91 520 | 26 000 | 117 520 |
| 3 | 96 160 | 36 400 | 132 560 |
| 4 | 130 120 | 52 000 | 182 120 |
| 5 | 134 600 | 67 600 | 202 200 |
| 6 | 147 320 | 104 000 | 251 320 |

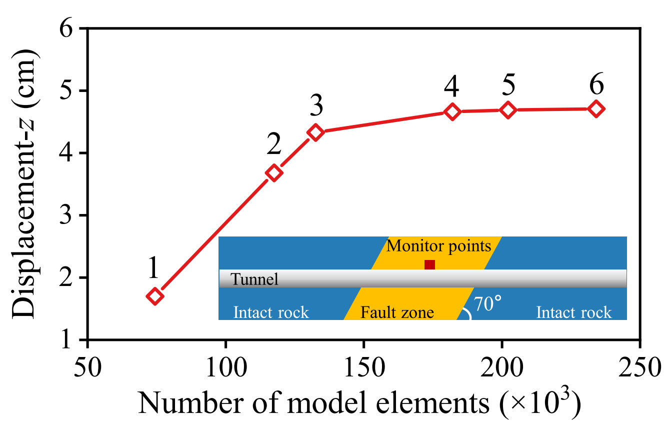


Fig. 5. Variation curve of the vertical displacement at the tunnel crown under different elements (blocks) densities.

pling model was developed based on the experimental prototype by Wang (2023), as illustrated in Fig. 6. It is crucial to emphasize that this model is solely used to verify the rationality and effectiveness of the proposed continuum-discrete coupling model, while subsequent parametric analyses will continue to use the model shown in Fig. 2.

Figure 7 compares the measured and simulated vertical displacements of the tunnel crown and invert, as well as their relative displacements. The results show that the experimental and numerical peak values of the vertical displacements at the tunnel crown and invert are almost identical, and the axial displacement variation along the tunnel exhibits an S-shaped pattern in both cases. However, there is a slight discrepancy between the experimental and numerical simulations: the peak relative displacement occurs at FP in the simulation, while in the experiment, it appears between FP and FB1. Despite this difference, the peak values of the relative displacement between the crown and invert remain similar.

To validate the rationality of the simulated tunnel damage pattern obtained from this study, the simulated tunnel damage is compared with the seismic damage of Longchi tunnel observed in 2008 Wenchuan earthquake in China, as shown in Fig. 8. During the 2008 Wenchuan earthquake, the secondary fault crossed by the Longchi Tunnel subject to reverse faulting, causing cracking and spalling of the concrete at the tunnel sidewalls. The numerical simulation results indicate that the tunnel crossing the reverse fault experienced significant damage due to the combined effects of axial compression and shear along the fault plane, which is consistent with the seismic damage mechanism observed in the Longchi Tunnel. However, due to the simplification of the tunnel structure in the model, which excluded structural details such as the support system, reinforcement, and flexible joints, discrepancies arise between the simulated tunnel damage and the actual seismic damage. For instance, the model fails to capture the misalignment phenomenon between tunnel segments. Overall, the coupling model proposed in this study effectively simulates tunnel damage under reverse faulting.

## 4 Parametric study on mechanical response of tunnels

The mechanical response and failure modes of cross-fault tunnels are influenced by multiple factors. Dowding and Rozen (1978) conducted a survey on the seismic damage of 78 rock tunnels in the United States and Japan, revealing that the extent of tunnel damage is closely related to the fault displacement magnitude. In practical seismic design for cross-fault tunnels, fault displacement is consid-

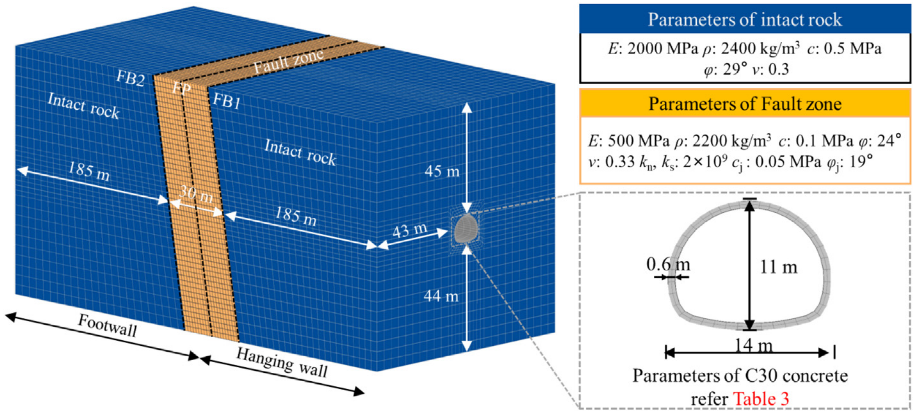


Fig. 6. Coupling model of the model test.

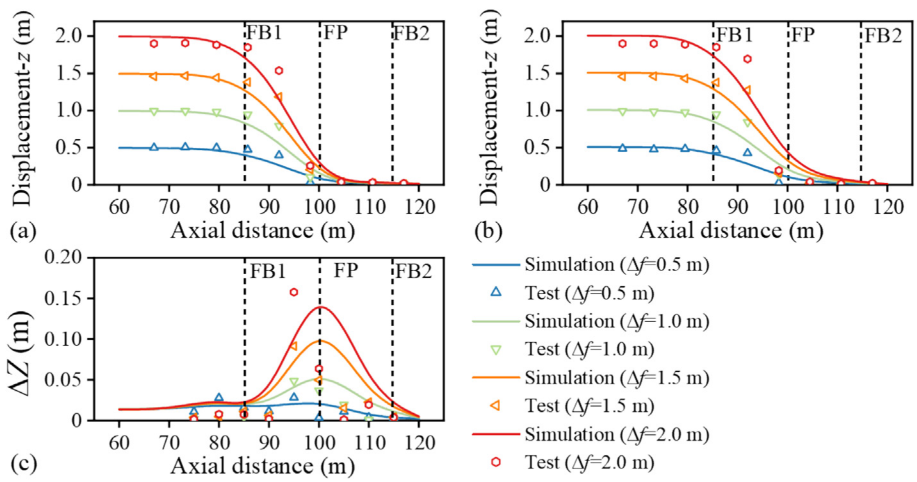


Fig. 7. Comparison between simulation results and test data. (a) Vertical displacement of tunnel crown, (b) vertical displacement of tunnel invert, and (c) vertical relative displacement between crown and invert.

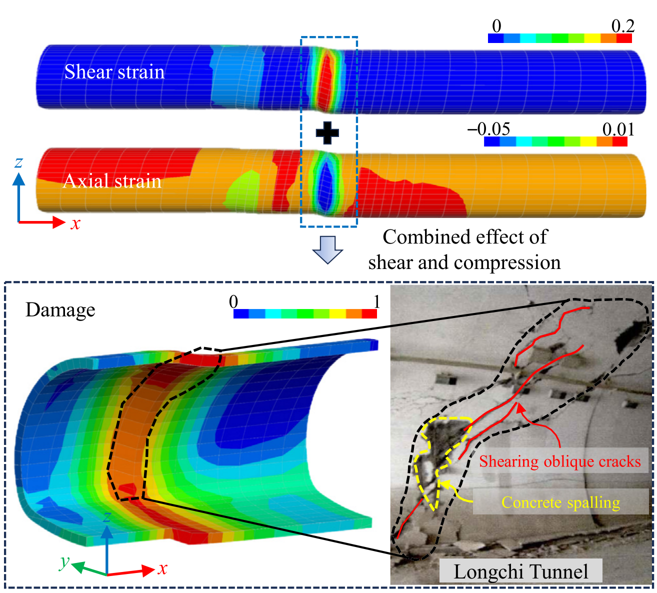


Fig. 8. Comparation between damage patterns of Longchi Tunnel and simulation results.

ered a key factor (Wang et al., 2024). Hashash (2001) highlighted that seismic damage to tunnels crossing faults should account for both fault displacement and fault width. Xin et al. (2024) conducted a systematic analysis of tunnel damage during the Wenchuan and Menyuan earthquakes, proposing that variations in fault width significantly affect the distribution of tunnel damage. Additionally, fault dip angle and the quality of fault zone rock mass also play a critical role in the mechanical response of tunnels. Qiao et al. (2022) and Zhong et al. (2020) have conducted detailed studies on fault dip angle and fault zone rock mass properties, respectively. In summary, the effects of fault displacement ($\Delta f$), fault dip angle ($\alpha$), fault width ($W_F$), and fault zone rock mass qualities ($Q_{fault}$) on the mechanical response of tunnels under reverse faulting are discussed in this section. The numerical cases are listed in Table 5. The mechanical parameters of different $Q_{fault}$ are listed in Table 6. Hard and medium correspond to grade V surrounding rock, and soft corresponds to grade IV surrounding rock.

Table 5
Numerical cases of parametric analysis.

| Case. | $\Delta f$ (m) | α (°) | $W_F$ | $Q_{fault}$ |
|---|---|---|---|---|
| 1 | 0.2, 0.3, 0.4, 0.5, 1.0, 2.0 | 70 | $2d$ | Medium |
| 2 | 0.5 | 50/60/70/80/90 | $2d$ | Medium |
| 3 | 0.5 | 70 | $1d$, $2d$, $3d$, $4d$, $5d$ | Medium |
| 4 | 0.5 | 70 | $2d$ | Hard/medium/soft |

Note: $d$ represents the outer diameter of tunnels.

Table 6
Mechanical parameter of different fault zone rock mass qualities (Zhong et al., 2020).

| $Q_{fault}$ | Rock mass mechanical parameters | | | | | Joint mechanical parameters | | | |
|---|---|---|---|---|---|---|---|---|---|
| | $E$ (MPa) | $\rho$ (kg·m$^{-3}$) | $v$ | $c$ (MPa) | $\varphi$ (°) | $k_n$ (GPa/m) | $k_s$ (GPa/m) | $c_j$ (MPa) | $\varphi_j$ (°) |
| Hard-2 | 5000 | 2300 | 0.30 | 0.70 | 37 | 67 | 67 | 0.350 | 18 |
| Hard-1 | 3800 | 2300 | 0.30 | 0.50 | 35 | 50 | 50 | 0.250 | 17 |
| Medium | 1500 | 2100 | 0.33 | 0.15 | 29 | 10 | 10 | 0.075 | 15 |
| Soft-1 | 1200 | 1900 | 0.37 | 0.13 | 25 | 10 | 10 | 0.065 | 13 |
| Soft-2 | 1000 | 1800 | 0.40 | 0.10 | 22 | 10 | 10 | 0.050 | 11 |

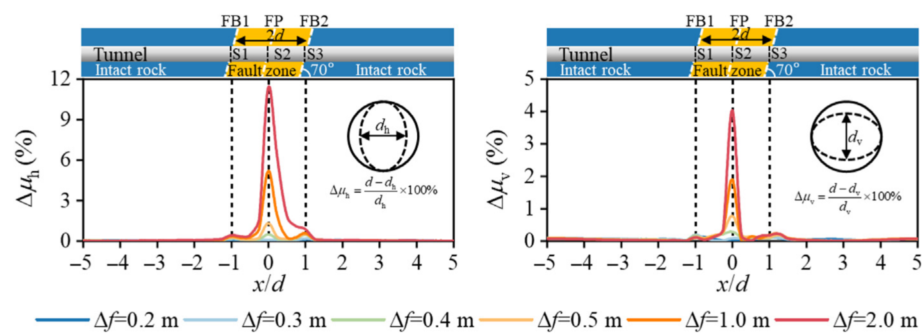


Fig. 9. Variations in transverse and vertical diametric deformation rates ($\Delta\mu_h$, $\Delta\mu_v$) of the tunnel along its axis under different fault displacement magnitudes ($\alpha = 70°$, $W_F = 2d$, $Q_{fault}$ = Medium). The distance from the tunnel axis to the fault plane is normalized by the tunnel diameter $d$. S1 ($x/d = -1$), S2 ($x/d = 0$), and S3 ($x/d = 1$) correspond to tunnel cross-sections near the FB1, FP, and FB2, respectively.

### 4.1 Influence of fault displacement magnitudes

Figure 9 illustrates the variation of the horizontal and vertical diametric deformation rates of the tunnel along its longitudinal direction under different fault displacements. It can be observed that the deformation rates of both the horizontal and vertical diameters progressively amplify with increasing fault displacement. The most significant deformation occurs at section S2 of the tunnel near FP. When the fault displacement reaches 2 m, the horizontal and vertical diameter deformation rates can reach 11% and 4%, respectively.

To intuitively evaluate the damage state of the tunnel lining, the damage volume ratio ($R_d$) of the tunnel cross-section is used as an evaluation metric. $R_d$ is defined as the ratio of the sum of the product of the volume and damage factor of each element within a cross-section to the total volume of the elements in the section, which can be calculated using Eq. (11):

$$R_d = \sum_{i=1}^{n}\left[D_i \cdot \left(V_i \middle/ \sum_{i=1}^{n} V_i\right)\right] \quad D_i = D_c, D_t, \tag{11}$$

where $D_i$ is the damage factor of the $i$-th element, $V_i$ is the volume of the $i$-th element, and $n$ is the total number of elements in the tunnel cross-section. In the concrete damage model, the lining damage is categorized into compressive damage $D_c$ and tensile damage $D_t$. Accordingly, the $R_d$ can be further divided into the damage volume ratio in compression ($R_{dc}$) and the damage volume ratio in tension ($R_{dt}$), to characterize the compression damage and tensile damage of tunnels, respectively.

Figure 10 illustrates the axial variation curves of the $R_{dc}$ and $R_{dt}$ of the tunnel lining under different fault displacement magnitudes (Fig. 10(a)) and the corresponding compressive and tensile damage contour diagrams (Fig. 10 (b)). It can be observed that under reverse fault displacement, tunnel damage is predominantly compressive damage, with its severity and distribution range significantly

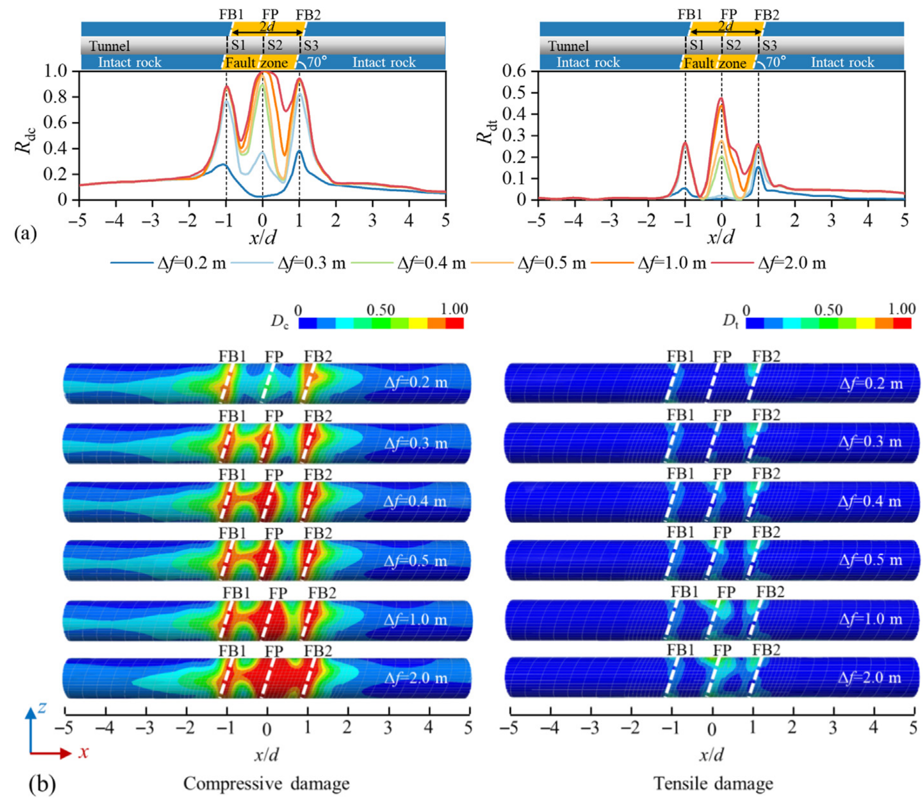


Fig. 10. Tunnel damage under different fault displacement magnitudes ($W_F = 2d$, $\alpha = 70°$, $Q_{fault}$ = Medium). (a) $R_{dc}$ and $R_{dt}$ variation curves along the tunnel axis, and (b) compressive and tensile damage contour diagrams.

exceeding those of tensile damage. The primary damage is concentrated near FB1/FB2 and FP, with the main affected range of $-1.5 < x/d < 1.5$. Wherein the damage at FP is relatively large. On the other hand, tensile damage mainly occurs at the tunnel crown with the most significant tensile damage observed at the tunnel crown on the hanging wall near FP.

The fault displacement magnitude significantly influences the extent and distribution of tunnel damage. In the stage of fault displacement $\Delta f$ is 0.2 m, compressive damage primarily appears at S1 and S3 (the peak $R_{dc}$ is 0.4), while no damage is observed at S2. When the fault displacement increases to 0.4 m, the damage at S2 escalates sharply, with the $R_{dc}$ of S1, S2, and S3 all reaching 0.8. As the fault displacement increases further to 0.5 m, S1, S2, and S3 near the fault undergo almost complete failure. Compressive damage appears at the tunnel sidewalls within the hanging wall fault zone ($-1 < x/d < 0$). With a further increase in displacement, the compressive damage zone within the footwall fault zone expands significantly.

It is evident that the tunnel near the fault zones is the weak segment where tunnel damage is most likely to occur, particularly at the fault zone boundaries (FB1 and FB2) and FP. In tunnel design and construction, emphasis should be placed on enhancing the shear and compressive resistance of the fault boundaries and fault plane.

### 4.2 Influence of fault widths

Figure 11 illustrates the variation of the horizontal and vertical diametric deformation rates along the longitudinal axis of the tunnel under different fault widths. The lateral deformation of the tunnel is significantly greater than the vertical deformation, and both show similar trends in response to changes in fault zone width. When the fault width is $1d$, the deformation of the tunnel at S2 reaches its maximum, with a $\Delta\mu_h$ and $\Delta\mu_v$ of 1.6% and 0.8%, respectively. As the fault width increases, the deformation characteristics of the tunnel in the hanging wall fault zone and footwall fault zone exhibit significant differences. Specifically, in the hanging wall fault zone (between S1 and S2), the tunnel deformation increases significantly with the widening of the fault, whereas in the footwall fault zone (between S2 and S3), the tunnel deformation demonstrates a decreasing trend. When the fault width reaches $5d$, the $\Delta\mu_h$ in the hanging wall fault zone reaches approximately 0.4%, while the $\Delta\mu_v$ approaches zero. Meanwhile, in the footwall fault zone, $\Delta\mu_h$ remains within the range of 0.2%–0.4%, and the $\Delta\mu_v$ also decreases to nearly zero.

Figure 12 illustrates the axial variation curves of the $R_{dc}$ and $R_{dt}$ of the tunnel lining under different fault widths (Fig. 12(a)) and the corresponding compressive and tensile

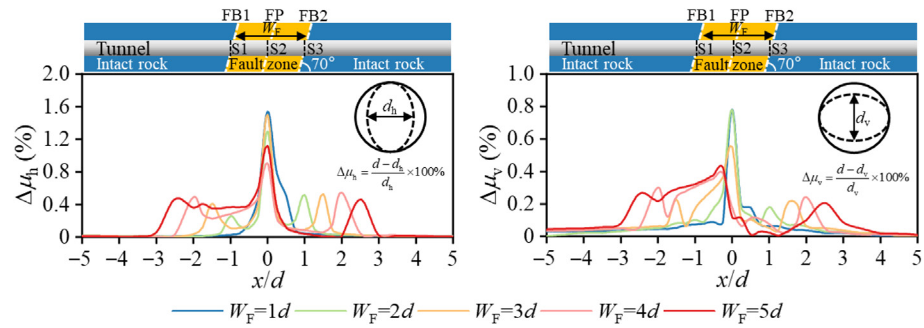


Fig. 11. Variations of transverse and vertical diametric deformation rates ($\Delta\mu_h$, $\Delta\mu_v$) of the tunnel along its axis under different fault widths ($\Delta f = 0.5$ m, $\alpha = 70°$, $Q_{fault}$ = Medium).

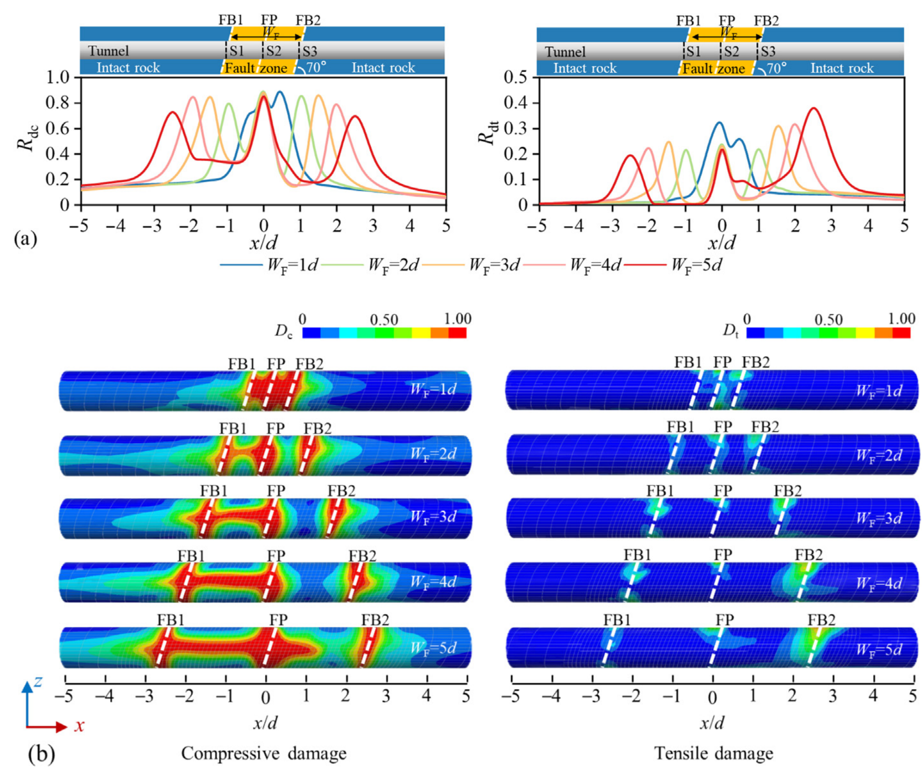


Fig. 12. Tunnel damage under different fault widths ($\Delta f = 0.5$ m, $\alpha = 70°$, $Q_{fault}$ = Medium). (a) $R_{dc}$ and $R_{dt}$ variation curves along the tunnel axis, and (b) compressive and tensile damage contour diagrams.

damage contour diagrams (Fig. 12(b)). At a fault zone width of 1$d$, the tunnel exhibits almost entirely compressive damage and minimal tensile damage in the fault zone. With the increase of fault width, the $R_{dc}$ demonstrates an overall decreasing trend at both S1 and S3, while the $R_{dt}$ exhibits a slight decrease at S1 and a pronounced increase at S3. Specifically, when the fault width increases from 1$d$ to 5$d$, the $R_{dc}$ at S3 represents a reduction of approximately 16% (from 0.89 to 0.75), while the $R_{dt}$ represents a 33% increase (from 0.3 to 0.4). Damage contours analysis further reveals that the compressive damage is primarily concentrated in stress concentration interface (FB1, FP and FB2), and the tunnel sidewalls within the hanging wall fault zone; tensile damage is mainly distributed in the tunnel crown near the FB2. Notably, the damage extent and affected range of these critical locations show a positive correlation with fault width, and their evolutionary patterns are in strong agreement with the quantitative trends observed in $R_{dc}/R_{dt}$ variations.

Integrating the tunnel deformation and damage observations, the influence mechanism of fault widths on tunnels can be explained as follows: when the fault width is small, the fault zone can be approximated as a fault plane, where the tunnel is mainly affected by concentrated shear displacements, resulting in more significant deformation. As the fault width increases, more fault displacement is absorbed by the fault zone, reducing the concentrated shear at the fault plane. Consequently, tunnel deformation and damage gradually extend toward to the FB1, FB2 and the areas between the FP and FB1/FB2.

Therefore, when a tunnel crosses a narrow fault zone, the shear resistance of the tunnel structure should be enhanced or reinforcing the rock mass in fault zone through grouting to effectively control deformation. For wide fault zones, focus should be directed toward strengthening the compressive and tensile resistance of the boundary areas to ensure structural stability and safety.

### 4.3 Influence of fault dip angles

Figure 13 illustrates the variation curves of horizontal and vertical diameter deformation rates of the tunnel along its longitudinal direction under different fault dip angles. For a fault dip angle of 50°, significant tunnel deformation occurs near the S1 and S3, with $\Delta\mu_h$ and $\Delta\mu_v$ reaching 1.0% and 1.5%, respectively. Furthermore, noticeable tunnel deformation persists within the footwall intact rock of $1 < x/d < 3$, where $\Delta\mu_h$ and $\Delta\mu_v$ range from 0.1% to 0.3% and 0.15% to 0.80%, respectively. This indicates that low dip angle faults exert a broader influence on tunnel deformation. As the fault dip angle increases (from 60° to 80°), significant deformation becomes increasingly concentrated within the fault zone. Consequently, deformation at S1 and S3 decreases markedly, while deformation at S2 increases substantially. Notably, for a dip angle of 70°, $\Delta\mu_h$ and $\Delta\mu_v$ at S2 reach 1.30% and 0.75%, respectively. However, under the extreme condition of a 90° fault dip angle, the tunnel deformation characteristics exhibit significant changes: the peak deformation zone shifts to the region between S1 and S2 ($-1 < x/d < 0$), rather than at S2, with peak values of horizontal deformation $\Delta\mu_h$ and $\Delta\mu_v$ reaching 1.0% and 1.3%, respectively.

Figure 14 shows the $R_{dc}$ and $R_{dt}$ of the tunnel under different fault dip angles (Fig. 14(a)) and the corresponding compressive and tensile damage contour diagrams (Fig. 14(b)). It can be observed that the damage patterns of the tunnel are generally consistent with its deformation patterns. When the fault dip angle is 50°, significant compressive damage is observed at FB1 and FB2 with the $R_{dc}$ reaching approximately 0.8. This damage extends approximately 3.5$d$ into the intact rock of the hanging wall. Significant tensile damage predominantly occurs near the tunnel crown at FB1 ($x/d = 0.8$) and within the intact rock mass of the hanging wall ($0.8 < x/d < 3.2$), particularly at the tunnel invert. This phenomenon arises because, under low dip angles (50°), the shear stress resulting from the relative displacement between the hanging wall and footwall generates a larger horizontal stress component, thereby reducing the sliding along the fault plane. Consequently, tunnel damage is concentrated at the interface between the fault and the intact rock, where significant stiffness changes occur, leading to stress concentration. Under significant horizontal stress, relative displacement occurs between the tunnel lining and the intact rock, resulting in more pronounced tensile damage at the crown in the hanging wall and the invert in the footwall. Furthermore, the extent of damage observed in the footwall is considerably more pronounced than that in the hanging wall. Additionally, the additional stress caused by fault instability at low dip angles exerts more pressure on the tunnel within the footwall, leading to much higher compressive damage in the footwall compared to the hanging wall.

As the increasing fault dip angle from 60° increases to 90°, both $R_{dc}$ and $R_{dt}$ at S2 exhibit a characteristic nonlinear trend of initial increase followed by decrease. Notably, $R_{dc}$ remains relatively stable at S1 and S3, while $R_{dt}$ at S1 demonstrates a more pronounced non-monotonic variation, characterized by an initial decrease followed by an increase. When the fault dip angle reaches 90°, the $R_{dt}$ value at S2 decreases to 0.45. When the dip angle reaches 90°, the longitudinal horizontal compressive damage in the sidewalls becomes markedly more pronounced, while tunnel crown damage in the range of $-0.8 < x/d < 0.8$ notably decreases, and the distribution of tensile damage remains slightly changed. This phenomenon can be attributed to the dominance of compressive stress under high dip angles, which simultaneously reduces shear stress along the FP. Tunnel failure is primarily influenced by axial compression and the vertical additional stress originating from the fault zone.

In summary, when a tunnel intersects with a low dip angle fault, it is crucial to reinforce the tensile performance of the tunnel invert at FB1 and FB2 to effectively mitigate tensile stress damage induced by fault dislocation. when a tunnel intersects with a high dip angle fault, the compressive strength of the tunnel sidewalls should be enhanced.

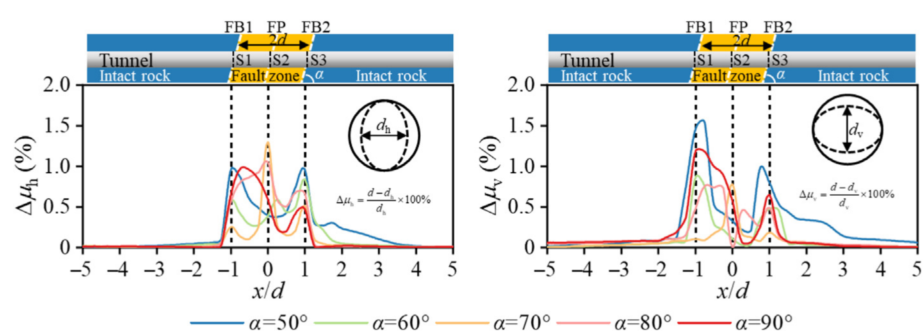


Fig. 13. Variations in transverse and vertical diametric deformation rates ($\Delta\mu_h$, $\Delta\mu_v$) of the tunnel along its axis under different dip angles ($\Delta f = 0.5$ m, $W_F = 2d$, $Q_{fault}$ = Medium).

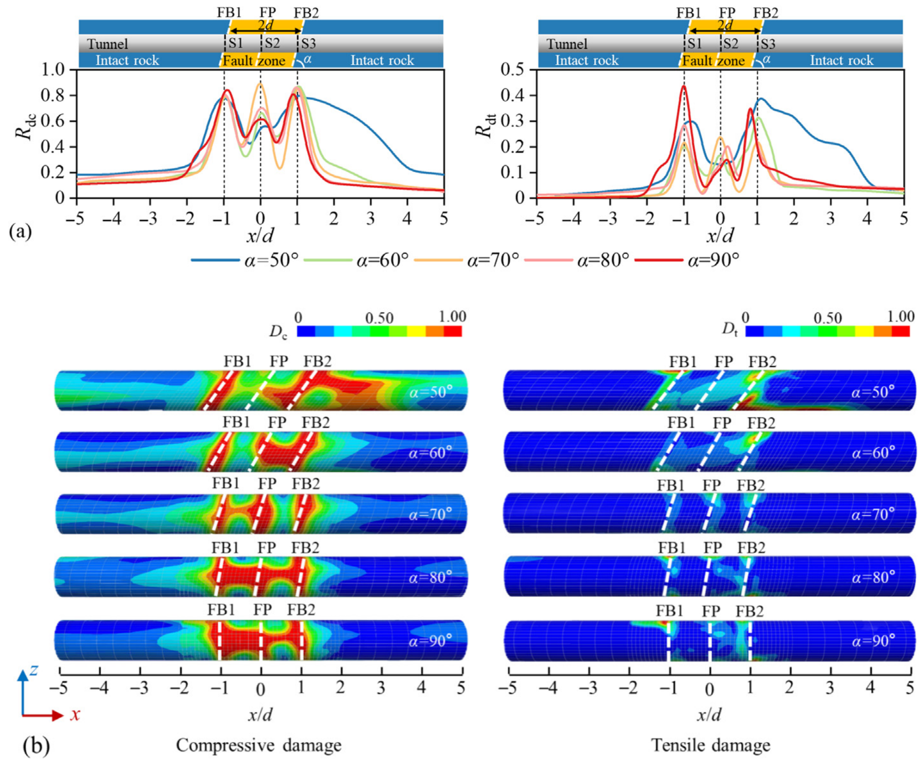


Fig. 14. Tunnel damage under different fault dip angles ($\Delta f = 0.5$ m, $W_F = 2d$, $Q_{fault}$ = Medium). (a) $R_{dc}$ and $R_{dt}$ variation curves along the tunnel axis, and (b) compressive and tensile damage contour diagrams.

The use of high-stiffness linings and anchoring measures is recommended to improve overall structural stability and resist damage caused by axial and vertical stresses.

## 4.4 Influence of fault zone rock mass qualities

Figure 15 illustrates the variation curves of the transverse and vertical diametric deformation rates of the tunnel along its longitudinal direction under different fault zone rock mass qualities. It can be observed that the tunnel deformation at S2 exhibits a continuous increase with the growing hardness of the fault zone rock mass, $\Delta\mu_h$ and $\Delta\mu_v$ reaching peak values of 2.2% and 1.5%, respectively. Conversely, the tunnel deformation patterns at S1 and S3 demonstrate an inverse trend, showing a gradual decrease with the improvement of rock mass quality.

Figure 16 illustrates the $R_{dc}$ and $R_{dt}$ of the tunnel under different fault zone rock mass qualities (Fig. 16(a)) and the corresponding compressive and tensile damage contour diagrams (Fig. 16(b)). The results demonstrate that the degradation of fault zone rock mass quality exerts a significant influence on the damage evolution in the crucial cross-sections for the tunnel (S1–S3). As the rock mass quality deteriorates from Hard-2 to Soft-2, there are significant differences in the damage conditions of each section. $R_{dc}$ at S1 represents a 197% increase (from 0.32 to 0.95), whereas $R_{dc}$ at S2 shows a 19% reduction (from 0.99 to 0.80), and S3 remains stable. The $R_{dt}$ at S1 and S3 demon-

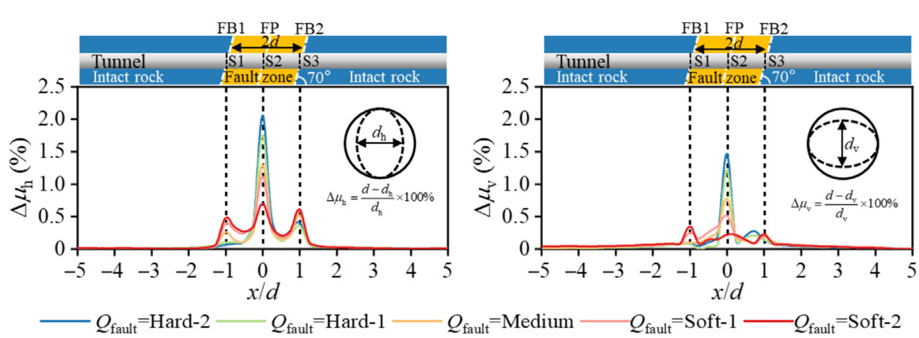


Fig. 15. Variations of transverse and vertical diameter deformation rates ($\Delta\mu_h$, $\Delta\mu_v$) of the tunnel along its axis under different fault zone rock mass qualities ($\Delta f = 0.5$ m, $W_F = 2d$, $\alpha$ = 70°).

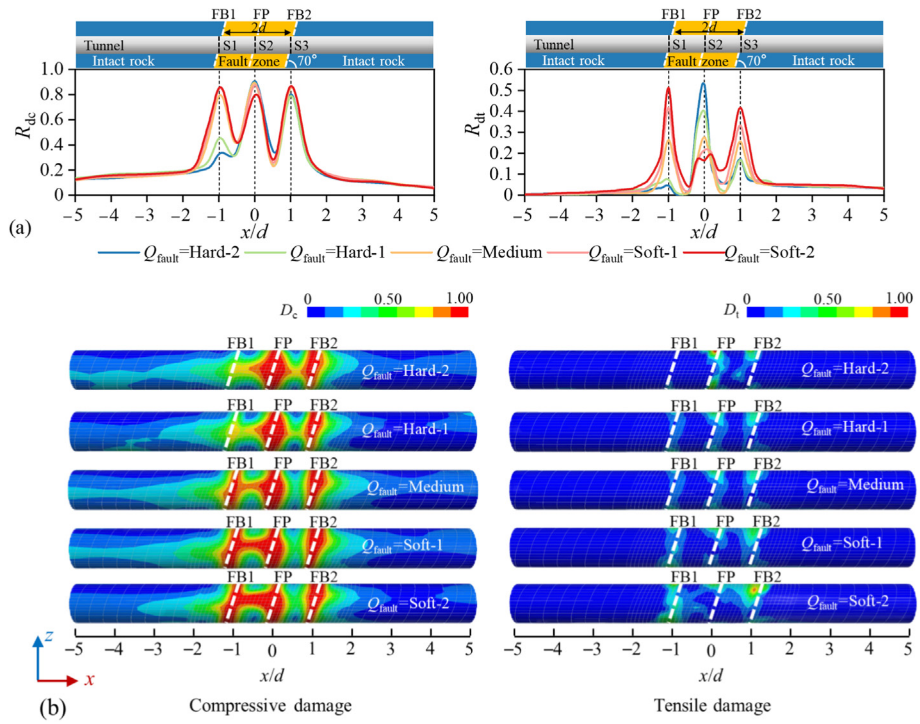


Fig. 16. Tunnel damage under different fault zone rock mass qualities ($\Delta f = 0.5$ m, $W_F = 2d$, $\alpha = 70°$). (a) $R_{dc}$ and $R_{dt}$ variation curves along the tunnel axis, and (b) compressive and tensile damage Contour diagrams.

strate significant increases of 940% (from 0.05 to 0.52) and 133% (from 0.18 to 0.42), respectively, while $R_{dt}$ at S2 shows a notable reduce of 62% (from 0.52 to 0.20). Further analysis of the damage contour diagrams reveals spatial heterogeneity in tunnel damage. The deterioration of rock mass quality leads to progressive expansion of compressive damage at FB1 and the tunnel sidewall, whereas the compressive damage at FP and FB2 remains relatively unchanged. Tensile damage at FB1/FB2 exhibits significant expansion and intensification of damage with increasing degradation, while the tensile damage at FP becomes concentrated near the crown, and the tensile damage in the sidewall region gradually diminishes.

Based on the deformation and damage characteristics of the tunnel, the effects of fault zone rock mass quality can be explained as follows: When the fault zone rock mass has higher hardness, the shear effects at the FP are stronger, resulting in the most severe deformation and damage at S2. Meanwhile, due to the relatively small stiffness difference between the fault zone and the intact surrounding rock, deformation primarily concentrates at S2, with less deformation occurring at S1. As the rock mass quality deteriorates, the shear effects at the fault surface weaken, and the stiffness difference between the fault zone and the intact surrounding rock increases. Consequently, deformation gradually shifts from the FP to FB2, leading to enhanced deformation at S1 and reduced deformation at S2.

For fault zones with poor rock mass quality, zonal reinforcement measures should be implemented. Particularly at the interface between soft and hard media, grouting or shotcrete reinforcement can be employed to enhance the strength of the surrounding rock, effectively mitigating the adverse effects of rock stiffness variation on tunnel structures.

## 5 Conclusions

This study established a continuous-discontinuous coupled model incorporating intact rock mass, fault zones, and tunnel. The non-uniform fault displacement was adopted as the input to simulate the mechanical response and damage patterns of tunnels crossing active faults under reverse faulting. The simulation results were validated by comparing them with observed tunnel damage from post-earthquake, as well as the laboratory tests. The results indicate that the coupled model effectively reproduces the failure modes of tunnels under reverse faulting, confirming the validity the coupling model. Furthermore, the close agreement between the simulation results and experimental data demonstrates the high computational accuracy and reliability of the coupling model. A systematic parametric analysis was conducted to investigate the effects of fault displacement, fault width, fault dip angle, and fault zone rock mass qualities on the mechanical response and damage patterns of tunnels. The main conclusions are as follows.

(1) Fault displacement is a key factor influencing the tunnel damage. The damage begins at the fault zone boundaries and extends to the fault plane as the fault

displacement increases. At fault displacement of 0.5 m, the investigated tunnel near these regions is completely damaged, and the damage subsequently propagates throughout the fault zone.

(2) The fault width affects deformation and damage distribution of the tunnels. Narrow faults cause concentrated shear deformation of tunnels. Wider fault absorbs more fault displacement, and tunnel deformation and damage are mainly localized at fault zone boundaries and the fault plane, with minor effects in the other area.

(3) Fault dip angle significantly impacts the stress distribution of the tunnels. Low dip angles result in significant shear stress and tensile damage at the footwall invert and hanging wall crown, while high dip angles induce axial and vertical compressive stresses induced by instability in the fault zone rock mass, causing sidewall damage.

(4) Fault zone rock mass quality significantly affects tunnel performance. High-quality rock (greater stiffness) minimizes axial stiffness variation and damage at fault zone boundaries. As the quality of the rock mass decreases, the axial stiffness of the surrounding rock in the tunnel changes significantly, leading to increased damage at the fault zone boundaries. Meanwhile, the constraint effect of the surrounding rock on the tunnel is weakened resulting in a significant expansion of the tensile failure area of the tunnel within the fault zone.

This study provides a new perspective on tunnel failure mechanisms under reverse faulting. However, the proposed coupling model is relatively simplified, with the accuracy of the nonlinear characterization of rock mass materials requiring further improvement. Additionally, the stochastic distribution of joint in the fault zone has not been considered, and the velocity effects of fault displacement are neglected. Future research will focus on developing a more refined coupling model, incorporating the dynamic effects of fault displacement, with the aim of providing a more comprehensive understanding of the dynamic response and failure mechanisms of cross-fault tunnels under real earthquake scenarios.

## Data availability

The data that support the findings of this study are available from the corresponding author upon reasonable request.

## CRediT authorship contribution statement

**Zhenning Ba:** Supervision, Funding acquisition, Writing – review & editing, Conceptualization. **Yao Wang:** Methodology, Writing – original draft, Conceptualization, Software. **Zhiwei Fang:** Visualization, Software. **Dongqiao Li:** Writing – review & editing.

## Declaration of competing interest

The authors declare that they have no known competing financial interests or personal relationships that could have appeared to influence the work reported in this paper.

## Acknowledgement

This research was supported by the National Key Research and Development Program of China (Grant No. 2023YFC3007403), which the authors gratefully acknowledged.

## References

Ahmadi, M., Moosavi, M., & Jafari, M. K. (2018). Experimental investigation of reverse fault rupture propagation through wet granular soil. *Engineering Geology, 239*, 229–240.

Anastasopoulos, I., Gazetas, G., Bransby, M. F., Davies, M. C. R., & El Nahas, A. (2007). Fault rupture propagation through sand: Finite element analysis and validation through centrifuge experiments. *Journal of Geotechnical and Geoenvironmental Engineering, 133*(8), 943–958.

Asakura, T., & Sato, Y. (1998). Mountain tunnels damage in the 1995 Hyogoken-Nanbu Earthquake. *Quarterly Report of RTRI, 39*(1), 9–16.

Cai, Q. P., Peng, J. M., Ng, C. W. W., Shi, J. W., & Chen, X. X. (2019). Centrifuge and numerical modelling of tunnel intersected by normal fault rupture in sand. *Computers and Geotechnics, 111*, 137–146.

Chen, P. L., Geng, P., Chen, J. B., & Gu, W. Q. (2023). The seismic damage mechanism of Daliang tunnel by fault dislocation during the 2022 Menyuan Ms6.9 earthquake based on unidirectional velocity pulse input. *Engineering Failure Analysis, 145*, 107047.

Chang, Y. Y., Lee, C. J., Huang, W. C., Hung, W. Y., Huang, W. J., Lin, M. L., & Chen, Y. H. (2015). Evolution of the surface deformation profile and subsurface distortion zone during reverse faulting through overburden sand. *Engineering Geology, 184*, 52–70.

Cui, Z., Li, J. H., Fu, X. W., Shen, Q., Zhou, G. X., Ma, Y., & Wang, T. Q. (2022). Evaluating the response of a tunnel subjected to strike slip fault rupture in conjunction with model test and hybrid discrete–continuous numerical modeling. *Rock Mechanics and Rock Engineering, 55*(8), 4743–4764.

Dowding, C. H., & Rozen, A. (1978). Damage to rock tunnels from earthquake shaking. *Journal of Geotechnical Engineering Division, 104*(2), 175–191.

Fei, J. B., Wei, J. Y., Khalid, M. I., Zhou, X. S., Li, G. L., & Chen, X. S. (2024). Failure of Daliang tunnel induced by active stick-slip faulting. *Journal of Rock Mechanics and Geotechnical Engineering*. https://doi.org/10.1016/j.jrmge.2024.07.007 (In Press).

Gao, J. Q., Wang, Q. Y., Wang, R., Yang, J., & Yang, Y. W. (2024). Model test study on the deformation and failure characteristics of mountain tunnel under a strike-slip fault dislocation. *Structures, 60*, 105903.

Gou, Y. X., Huang, Q. B., Kang, X. S., Wang, L. X., Yang, X. Q., & Teng, H. Q. (2023). Experimental study on the mechanical response of metro shield tunnels obliquely crossing ground fissures. *Tunnelling and Underground Space Technology, 132*, 104849.

Hashash, Y. M. A., Hook, J. J., Schmidt, B., & I-Chiang Yao, J. (2001). Seismic design and analysis of underground structures. *Tunnelling and Underground Space Technology, 16*(4), 247–293.

Huang, J. Y. (2016). *Research on the method for evaluating the earthquake surface rupture*. [Doctoral dissertation, Institute of Engineering Mechanics, China]. (in Chinese).

Itasca. (2022a). FLAC3D User's Manual. Itasca Consulting Group, version 9.0. USA.

Itasca. (2022b). 3DEC User's Manual. Itasca Consulting Group, version 9.0. USA.

Kiani, M., Ghalandarzadeh, A., Akhlaghi, T., & Ahmadi, M. (2016a). Experimental evaluation of vulnerability for urban segmental tunnels subjected to normal surface faulting. *Soil Dynamics and Earthquake Engineering, 89*, 28–37.

Kiani, M., Akhlaghi, T., & Ghalandarzadeh, A. (2016b). Experimental modeling of segmental shallow tunnels in alluvial affected by normal faults. *Tunnelling and Underground Space Technology, 51*, 108–119.
Li, H. Y., Li, X. G., & Liu, H. (2023). Deformation and failure mechanism of metro shield tunnel subjected to buried fault dislocation. *Engineering Failure Analysis, 153*, 107551.
Li, H. Y., Li, X. G., Yang, Y., Liu, Y., & Ma, M. Z. (2022). Structural stress characteristics and joint deformation of shield tunnels crossing active faults. *Applied Sciences, 12*(7), 3229.
Liu, W., Huang, C. J., Zhang, S. F., & Song, Z. Y. (2023). Centrifuge tests of large-diameter steel pipes crossing strike-slip faults. *Engineering Structures, 279*, 115124.
Lin, M. L., Chung, C. F., Jeng, F. S., & Yao, T. C. (2007). The deformation of overburden soil induced by thrust faulting and its impact on underground tunnels. *Engineering Geology, 92*(3–4), 110–132.
Liu, Y. Q., Yao, C. F., Luo, W., He, C., Sun, M. H., Wang, E. L., & Yuan, F. Y. (2024). Deformations and damages of tunnels subjected to strike-slip faulting: Effects of tectonic stress and cross-sectional shape. *Engineering Failure Analysis, 160*, 108159.
Ma, Y., Sheng, Q., Zhang, G. M., & Cui, Z. (2019). A 3D discrete-continuum coupling Approach for investigating the deformation and failure mechanism of tunnels across an active fault: A case study of Xianglushan tunnel. *Applied Sciences, 9*(11), 2318.
O'Rourke, T. D., & Bonneau, A. L. (2007). Lifeline performance under extreme loading during earthquakes. In *Earthquake geotechnical engineering* (pp. 407–432). Springer.
Owen, G. N., & Scholl, R. E. (1981). *Earthquake engineering of large underground structures*. Federal Highway Administration, Report No. FHWA/RD-80/195.
Prentice, C. S., & Ponti, D. J. (1997). Coseismic deformation of the Wrights tunnel during the 1906 San Francisco earthquake: A key to understanding 1906 fault slip and 1989 surface ruptures in the southern Santa Cruz Mountains, California. *Journal of Geophysical Research - Solid Earth, 102*(B1), 635–648.
Qiao, Y. F., Tang, J., Liu, G. Z., & He, M. C. (2022). Longitudinal mechanical response of tunnels under active normal faulting. *Underground Space, 7*(4), 662–679.
Rahman, M. A., & Taniyama, H. (2015). Analysis of a buried pipeline subjected to fault displacement: A DEM and FEM study. *Soil Dynamics and Earthquake Engineering, 71*, 49–62.
Sabagh, M., & Ghalandarzadeh, A. (2020). Centrifugal modeling of continuous shallow tunnels at active normal faults intersection. *Transportation Geotechnics, 22*, 100325.
Shen, Y. S., Gao, B., Yang, X. M., & Tao, S. J. (2014). Seismic damage mechanism and dynamic deformation characteristic analysis of mountain tunnel after Wenchuan earthquake. *Engineering Geology, 180*, 85–98.
Tali, N., Lashkaripour, G. R., Moghadas, N. H., & Ghalandarzadeh, A. (2019). Centrifuge modeling of reverse fault rupture propagation through single-layered and stratified soil. *Engineering Geology, 249*, 273–289.
Tang, J., He, M. C., Bian, H. B., & Qiao, Y. F. (2024). A novel numerical framework to simulate mechanical response and damage characteristics of mountain tunnels under faulting. *Engineering Failure Analysis, 158*, 108030.
Tian, S. M., Wu, K. F., Yu, L., Li, X., Gong, J. F., & Wang, X. D. (2022). Key technology of anti-seismic for railway tunnels crossing active fault zone. *Tunnel Construction, 42*(8), 1351–1364 (in Chinese).
Wang, Q., Geng, P., Li, P. S., Wang, T. Q., & Sun, W. H. (2023a). Failure analysis and dislocation-resistant design parameters of mining tunnel under normal faulting. *Engineering Failure Analysis, 143*, 106902.
Wang, Q., Geng, P., Li, P. S., He, D. W., & Shen, H. M. (2024). Failure analysis of circumferential joints and preferable bolt form of shield tunnel under normal fault dislocation. *Tunnelling and Underground Space Technology, 146*, 105648.
Wang, S. G. (2023). *Research on dislocation response and fault resistance performance of tunnel structures across active faults considering dislocation modes*. [Master's Thesis, Kunming University of Science and Technology, China]. (in Chinese).
Wang, T. Q., Geng, P., Liu, G. G., Chen, C. J., & Gu, W. Q. (2023b). Performance-based three-level fortification goal and its application in anti-dislocation countermeasures: A case study of Shantou Submarine tunnel. *Underground Space, 12*, 251–270.
Wang, W. L., Wang, T. T., Su, J. J., Lin, C. H., Seng, C. R., & Huang, T. H. (2001). Assessment of damage in mountain tunnels due to the Taiwan Chi-Chi Earthquake. *Tunnelling and Underground Space Technology, 16*(3), 133–150.
Wang, Z., Zhong, Z. L., Zhao, M., Du, X. L., Huang, J. Q., & Wang, H. R. (2025). Experimental study on mechanical behavior and countermeasures of mountain tunnels under strike-slip fault movement. *Underground Space, 21*, 1–21.
Wang, Z. (2022). *Disaster mitigation and damage mechanism of rock tunnels with countermeasures crossing active fault zones*. [Doctoral dissertation, Beijing University of Technology, China]. (in Chinese).
Xin, C. L., Feng, W. K., Song, D. Q., Huang, S., & Liu, X. L. (2024). Seismic damage to non-fault-crossing and fault-crossing tunnels: Comparative study of the 2008 Wenchuan earthquake (Mw 7.9) and the 2022 Menyuan earthquake (Mw 6.7). *Engineering Failure Analysis, 166*, 108843.
Yang, H. H., Wang, M. N., Yu, L., & Zhang, X. (2024a). Analytical and numerical analysis on the mechanical response and damage characteristics of tunnels subjected to multiple normal faulting. *Computers and Geotechnics, 169*, 106254.
Yang, H. H., Wang, M. N., Luo, X., Yu, L., Zhang, X., & Tang, L. Z. (2024b). Longitudinal and cross-sectional partitioned failure mechanism of tunnels subjected to stick-slip action of strike-slip faults. *Journal of Central South University, 31*(1), 250–271.
Yao, C. F., He, C., Takemura, J., Feng, K., Guo, D. P., & Huang, X. (2021a). Active length of a continuous pipe or tunnel subjected to reverse faulting. *Soil Dynamics and Earthquake Engeering, 148*, 106825.
Yao, C. F., Takemura, J., Ma, G. Y., Dai, C., & An, Z. L. (2021b). Effect of boundary friction on revere fault rupture propagation in centrifuge tests. *Soil Dynamics and Earthquake Engineering, 147*, 106811.
Yao, C. F., Duan, J. N., Liu, Y. L., Luo, W., He, C., Yang, W. B., Zhang, J. C., & Xu, G. W. (2025). Damage and failure analysis of twin tunnels with cross passages subjected to strike-slip faulting. *Engineering Failure Analysis, 169*, 109197.
Yu, H. T., Chen, J. T., Bobet, A., & Yuan, Y. (2016). Damage observation and assessment of the Longxi tunnel during the Wenchuan earthquake. *Tunnelling and Underground Space Technology, 54*, 102–116.
Zhang, C. Q., Liu, X. Y., Zhu, G. J., Zhou, H., Zhu, Y., & Wang, C. (2020). Distribution patterns of rock mass displacement in deeply buried areas induced by active fault creep slip at engineering scale. *Journal of Central South University, 27*(10), 2849–2863.
Zhang, J. W., Cui, Z., Sheng, Q., Zhao, W. H., & Song, L. (2024). Experimental study on the effect of flexible joints of a deep-buried tunnel across an active fault under high in-situ stress conditions. *Underground Space, 19*, 189–207.
Zhang, X., Shen, Y. S., Qiu, J. T., Chang, M. Y., Zhou, P. F., Huang, H. F., & Zhu, P. L. (2024a). Failure and deformation mode for soil and tunnel structure crossing multiple slip surfaces of strike-slip fault in model test. *Soil Dynamics and Earthquake Engineering, 179*, 108541.
Zhang, X., Yu, L., Wang, M. N., & Yang, H. H. (2024b). Mechanical response and failure characteristics of tunnels subjected to reverse faulting with nonuniform displacement: Theoretical and numerical investigation. *Engineering Failure Analysis, 156*, 107809.
Zhang, Y., Zhang, Z. Q., Yin, C., Wei, R. H., & Zhang, H. (2023a). Experimental study on forced response characteristics and anti-dislocation performance of articulated tunnel structure under dislocation action of normal fault. *Structures, 48*, 867–881.
Zhang, Z. Q., Zhang, Y., Wei, R. H., Yin, C., & Zhang, H. (2023b). The damage mode and forced response characteristics of articulated lining structure: A case study of metro tunnel under a reverse fault action. *Tunnelling and Underground Space Technology, 140*, 105246.
Zhong, Z. L., Wang, Z., Zhao, M., & Du, X. L. (2020). Structural damage assessment of mountain tunnels in fault fracture zone subjected to multiple strike-slip fault movement. *Tunnelling and Underground Space Technology, 104*, 103527.